Smart Structures and Systems, Vol. 1, No. 4 (2005) 385-404
DOI: http://dx.doi.org/10.12989/sss.2005.1.4.385

Crack mapping in RC members using distributed coaxial cable crack sensors: modeling and application

Gary Greene, Jr.[†], Abdeldjelil Belarbi[‡] and Genda Chen[‡†]

Department of Civil, Architectural, and Environmental Engineering, University of Missouri-Rolla, 1870 Miner Circle, Rolla, MO 65409-0030, USA

(Received July 19, 2005, Accepted October 5, 2005)

Abstract. The paper presents a model to calculate reinforcement strain using measured crack width in members under applied tension, flexure, and/or shear stress. Crack mapping using a new type of distributed coaxial cable sensors for health monitoring of large-scale civil engineering infrastructure was recently proposed and developed by the authors. This paper shows the results and performance of such sensors mounted on near surface of two flexural beams and a large scale reinforced concrete box girder that was subjected to cyclic combined shear and torsion. The main objectives of this health monitoring study was to correlate the sensor's response to strain in the member, and show that magnitude of the signal's reflection coefficient is related to increases in applied load, repeated cycles, cracking, and reinforcement yielding. The effect of multiple adjacent cracks, and signal loss was also investigated. The results shown in this paper are an important step in using the sensors for crack mapping and determining reinforcement strain for in-situ structures.

Keywords: coaxial cable sensor; crack mapping; crack sensor; distributed sensors; strain.

1. Introduction

It is difficult to precisely characterize the internal condition of a reinforced concrete (RC) structure in service or after an extreme loading event such an earthquake. Information about the state of strain in the reinforcing bars can be estimated by direct measurement of crack width and spacing. Due to the inherent variability of crack spacing, the average of measurements across several cracks would be necessary to approach an accurate calculation. This method could not be used if the crack width spacing was changing due to changes in the internal stresses as is the case for most structures. Also visual inspection and measurement of surface crack patterns may not reveal the full extent of damage because gravity loads may close cracks, and other cracks may be hidden. Embedded electronic strain gages mounted on the reinforcing bars only give local information and are easily damaged. The process of structural evaluation can be simplified by using distributed sensors that can be installed along the entire length of a member. An innovative coaxial cable sensor has been developed for structural health monitoring in large-scale civil engineering infrastructure that is based on the change in topology of the outer conductor.

†Ph.D. Graduate Student, E-mail: ggg3kf@umr.edu
‡Distinguished Professor, Corresponding Author, E-mail: belarbi@umr.edu
‡†Associate Professor, E-mail: gchen@umr.edu

To significantly improve the sensitivity of previous coaxial cable sensors (Lin, *et al*. 2000), a new design was developed based on the change in topology, or electrical structure, of a coaxial cable. Research on small-scale flexural beams (Chen, *et al*. 2004, and McDaniel 2004), and on a large scale girder subjected to cyclic torsional loading (Chen, *et al*. 2003) validated this type of sensor of detecting and locating cracks in RC members.

In this study, a large scale RC box girder was tested under cyclic combined shear and torsion, to study the shear/torsion performance under cyclic loading. In addition, the study included the feasibility of using a coaxial cable as a measuring device, and a correlation between the sensor's response and strain in the member is made. The magnitude of the signal's reflection coefficient was related to increases in applied load, repeated cycles, crack opening/location, and yielding of the reinforcing bars. The effect of multiple adjacent cracks, and signal loss was also investigated.

2. Research significance

The model presented in this paper is an important step in using the cable sensors for crack mapping and calculating the strain in reinforcing bars. The application of the cable sensors in the flexural beams and full scale girder discussed in this paper is an important part of interpreting the sensor's response. Understanding how the signal response is affected by different types of loading, multiple cycles, and rebar yielding is necessary to make accurate predictions of crack widths and rebar strain. With continuous information like this along the length of multiple members, the evaluation of the structural condition of an entire structure could be made quickly and reliably.

3. Design and performance of topology-based sensors

3.1. Principle of ETDR

Electrical Time-Domain Reflectometry (ETDR) is a remote sensing technology based on the propagation of electromagnetic waves in an electrical cable or a transmission line, which functions both as a signal carrier and a sensor. It also involves the use of a digital sampling oscilloscope with an ETDR sampling head. The sampling instrument launches a series of low-amplitude and fast-rising step pulses onto the transmission line and samples the reflected signal caused by an electrical property change, i.e., a discontinuity, along the cable. The arrival time of the reflected signal includes the information of the distance between the points of monitoring and a discontinuity while the intensity of the signal represents the degree of the discontinuity. The amplitude of the reflected voltage wave normalized to that of the incident voltage wave is known as the reflection coefficient.

3.2. Design of topology-based sensors

The distributed crack sensors used in this study are actually coaxial cables. Two different designs of cables have been studied thus far. In the first design (Chen, *et al*. 2004), each sensor consists of a solid inner conductor, a spirally-wrapped copper-tape outer conductor, and a rubber tube in between the conductors as dielectric. This is referred to as a rubber sensor. It differs from a commercial coaxial

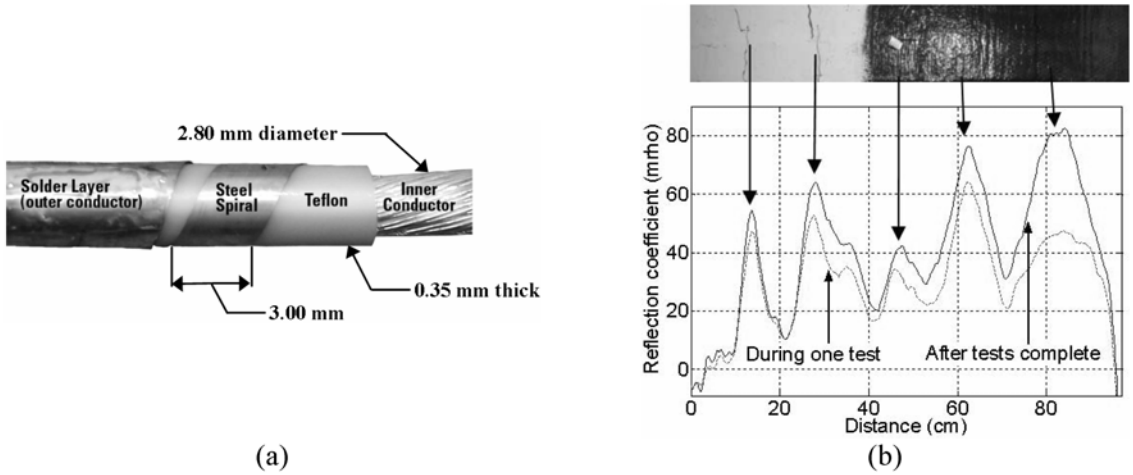

Fig. 1 (a) Cut-away sample of Teflon sensor and (b) differenced data captured during testing and memorized after tests

cable in that the topology of the outer conductor of the sensor can change with the onset of a crack in the concrete in which it is embedded.

The second design of crack sensors differs from the rubber sensors in the use of dielectric material and the fabrication process of their outer conductor. The new sensor is made up of an inner conductor, a rigid dielectric material, and an outer conductor which is coated with a layer of solder as can be seen in Fig. 1(a). The inner conductor is made up of copper wires surrounded with a PTFE (Teflon) dielectric. As such, the sensor is referred to as a Teflon sensor. The outer conductor of the sensor is a stainless steel spiral material. The spiral is wrapped without adhesive around the dielectric in such a way as to ensure that each turn of the spiral is touching edge to edge without any gap or overlapping. The spiral can therefore slide along the dielectric. A thin coat of solder is then applied evenly over the entire surface of the spiral enabling the spiral to remain in place and allow for a continuous axial current path over the surface of the outer conductor at zero loading. The solder is strong enough to hold the spirals in place while still allowing for the spirals to separate when the concrete surrounding the sensor cracks and pulls the spirals apart. This enables the outer conductor to be electrically continuous but mechanically separated. The sensors can be embedded in 13 mm by 13 mm channels in the near surface of RC members and grouted into the channel using a masonry grout. When the crack propagates across the channel containing the sensor, the grout also cracks with the member. The grout adheres to the outer conductor of the sensor and when the grout cracks, the spiral is separated.

3.3. Sensor performance: recoverability and crack memory

A cable sensor embedded in an RC member may be subjected to loading or unloading over time. Due to the introduction of a spiral outer conductor, a concern during the tests was that the sensor may not return to its original state corresponding to zero loading after the sensor is loaded and then unloaded. To describe this effect, a term denoted recoverability is introduced in this paper as defined by Eq. (1).

$$\text{Recoverability} = \left(1 - \frac{\text{peak value of reflection coefficent at zero load}}{\text{peak value of reflection coefficent at the previous peak load}}\right) \times 100\%$$

In one example (Chen, *et al*. 2003), the recoverability of a rubber sensor at the point of a crack was 87.5%. As more cracks or wider cracks develop with increasing stress, the recoverability decreases. It is noteworthy to mention that, in general, the cracks at zero twists in torsional members are not completely closed due to residual deformation.

Related to the recoverability of a sensor is the "memory" ability of a Teflon sensor for dynamic signals. In other words, the sensor is able to "remember" where the cracks had occurred after dynamic testing was completed. For example, after an RC column has been tested on a shake table, the peaks in the electronic signal from the sensor corresponding to cracking remained visible in the signal once testing was completed, while it was difficult to detect the cracks on the face of the column visually. Fig. 1(b) shows the signal from a column captured after testing was completed. It can be seen from Fig. 1(b) that the cracks that had opened during motion (one test) early in the test are still visible in the sensor signal after the tests are completed and higher displacement levels were achieved (McDaniel 2004).

4. Crack mapping model

The average strain in reinforcing bars of an RC beam can be easily calculated; however it is more difficult to calculate the strain at a crack. Previous expressions for reinforcement strain at a crack, such as the one developed by Gergely and Lutz (1968), were empirical. In Eq. (2), which is based on the Gergely-Lutz equation for maximum crack width, ε_{s0} is the strain in the reinforcing bars at the crack location, w_{max} is the maximum crack width, β is a factor accounting for strain gradient, d_c is the

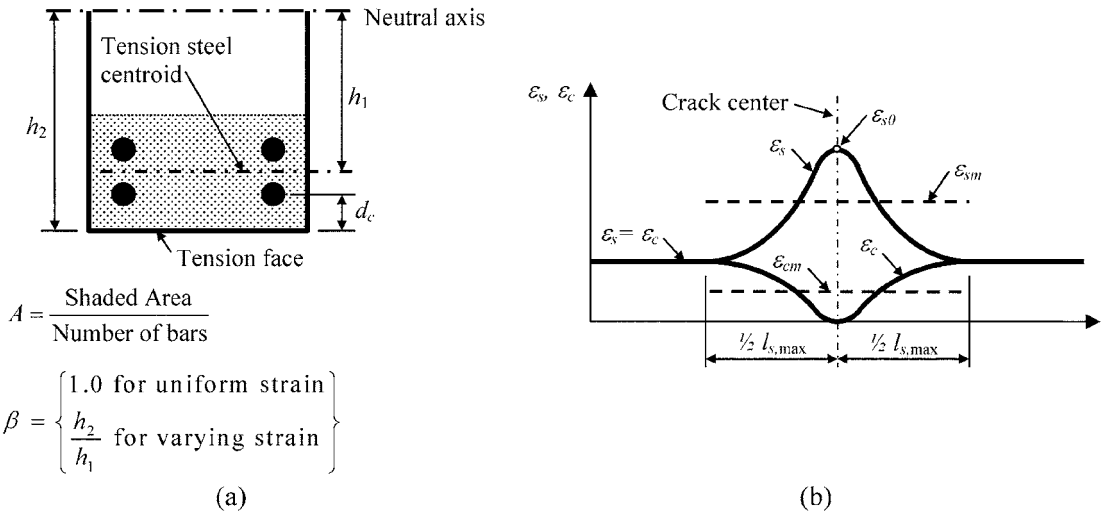

Fig. 2 (a) Parameter definitions for Gergely-Lutz equation and (b) strain distribution assumed in CEB-FIP Model Code 1990

distance from the extreme tension fiber to the center of the closest bar, and A is the effective area of concrete surrounding each bar (Fig. 2(a)). The strain in the reinforcing bars can be estimated by Eq. (2) using an experimentally measured crack width. The Gergely-Lutz equation was based on the statistical evaluation of the test data from six different experimental investigations. The specimens in the evaluation were loaded in either direct tension or flexure. The data did not include observations about yielding of the reinforcing bars. In general, the width of cracks is subject to relatively large scatter.

More recently, rational expressions have been derived which can predict the reinforcement strain at a crack and consider the tension stiffening effect of concrete. Belarbi and Hsu developed Eqs. (3-5) for the stress in the reinforcement at a crack, σ_{s0} (Belarbi and Hsu 1994). The first term in Eq. (3), σ_s, is the average stress in reinforcing bars. The second term, a_s, accounts for the tension stiffening effect of the concrete surrounding the reinforcing steel. a_s is defined in Eq. (4), where σ_r is the average tensile stress of reinforced concrete and ρ_s is the percentage of reinforcement based on the net concrete section. σ_r is calculated by Eq. (5), where f_{cr} and ε_{cr} are the stress and strain of concrete at cracking, and ε_r is the average principle tensile strain.

Considering the case where the reinforcing bars do not yield, the strain in the reinforcing bars at a crack, ε_{s0}, can be obtained by dividing Eq. (3) by the modulus of elasticity for steel, E_s. For this case, the average reinforcing steel strain is equal to the average principal tensile strain ($\varepsilon_r = \varepsilon_s$) which results in Eq. (6). A simple expression relating the average principal tensile strain to the average crack width, w_m, and to the average crack spacing is given by Eq. (7).

$$\varepsilon_{s0} = w_{\max} / (2.2\beta^3 \sqrt{d_c A}) \tag{2}$$

$$\sigma_{s0} = \sigma_s + a_s \tag{3}$$

$$a_s = \sigma_r / \rho_s \tag{4}$$

$$\sigma_r = f_{cr} (\varepsilon_{cr} / \varepsilon_r)^{0.4} \tag{5}$$

$$\varepsilon_{s0} = \varepsilon_r + a_s / E_s \tag{6}$$

$$\varepsilon_r = w_m / s_m \tag{7}$$

The reinforcing bars strain at a crack then becomes a matter of calculating the principal tensile strain. In the laboratory, the ε_r in a specimen can be measured using a series of LVDT's in the horizontal, vertical, and diagonal directions to create a smeared concrete strain sensor (SCSS). It is important to use several LVDT's that each span multiple cracks in order to obtain an accurate displacement measurement to calculate average strain (Belarbi and Hsu 1995).

Calculating ε_r from a member not equipped with the proper instrumentation is more difficult. In order to use Eq. (7), multiple crack widths and crack spacing measurements would need to be averaged. Alternately, the average crack width could be determined by summing the width of several cracks along a line orthogonal to the crack angle, and then dividing by the number of cracks. In the same manner the average spacing could be calculated from the length of the orthogonal line. However, this method would require calculations along several lines to approach an accurate calculation, and if the crack width/spacing was changing due to changes in the internal stresses, the method could not be used. To simplify this process, the next section will propose methods for estimating ε_r by using measured crack

width(s) and calculated crack spacing.

4.1. Average crack spacing based on CEB-FIP Model Code 1990

The European CEB-FIP Model Code 1990 (CEB-FIP 1993) defines the characteristic crack width, w_k, using Eq. (8). This crack width is the width that only 5% of the cracks will exceed. Fig. 2(b) shows the distribution assumed by the CEB-FIB Code for the reinforcing steel strain, ε_s, and concrete strain, ε_c, at a crack. $l_{s,\max,}$ is the length over which slip between the reinforcing steel and the concrete occurs, and ε_{sm} and ε_{cm} are the average reinforcing steel and concrete strains within $l_{s,\max}$. For stabilized crack growth, $l_{s,\max}$ is defined in Eq. (9), where d_b is the bar diameter and the reinforcement ratio, $\rho_{s,eff}$, is given in Eq. (10). For a slab or tension member, A_s is the cross-sectional area of the reinforcement and $A_{c,eff}$ is the effective concrete area calculated by assuming a concrete thickness of $2.5(c + 0.5d_b)$, where c is the concrete cover distance to the reinforcement. The CEB-FIB Code derives Eq. (11) for the mean strains ε_{sm} and ε_{cm}. β is an empirical factor to assess the average strain within $l_{s,\max}$ and $\varepsilon_{s,cr}$ is the strain in the reinforcing bars when the concrete first cracked. $\varepsilon_{s,cr}$ is given by Eq. (12).

$$w_k = l_{s,\max}(\varepsilon_{sm} - \varepsilon_{cm}) \tag{8}$$

$$l_{s,\max} = d_b/(3.6\rho_{s,eff}) \tag{9}$$

$$\rho_{s,eff} = A_s/A_{c,eff} \tag{10}$$

$$\varepsilon_{sm} - \varepsilon_{cm} = \varepsilon_{s0} - \beta\varepsilon_{s,cr} \tag{11}$$

$$\varepsilon_{s,cr} = f_{cr}/(\rho_{s,eff} E_s) \tag{12}$$

The average crack width w_m given in Eq. (13) can then be derived from Eqs. (8) and (11) and by taking w_m equal to 1.7 w_k. For stabilized cracks, the CEB-FIB Code assumes that $l_{s,\max,}$ is equal to the maximum crack spacing, $s_{\max}$. Based on this, Eq. (14) for the average crack spacing can then be defined and is a function of d_b, c, and the reinforcement ratio, ρ. Previous studies (Rizkalla, Hwang, and El Shahawi 1983, Beeby 1972, and Leonhardt 1977) developed equations for calculating crack spacing which were also a function of these variables.

The average principal tensile strain can now be calculated using Eq. (7) where w_m is calculated using the average of several measured crack widths along a crack, and s_m is calculated using Eq. (14). In addition, a modified form of the final term of Eq. (8), which accounts for the tension stiffening effect of concrete, can be derived from Eq. (13). Eq. (15) is derived by combining Eqs. (13) and (14) and then solving for ε_{s0}. In Eq. (15), the $\beta\varepsilon_{s,cr}$ term has replaced the a_s/E_s term of Eq. (8).

$$w_m = w_k/1.7 = (l_{s,\max}/1.7)(\varepsilon_{s0} - \beta\varepsilon_{s,cr}) \tag{13}$$

$$s_m = l_{s,\max}/1.7 \tag{14}$$

$$\varepsilon_{s0} = w_m/s_m + \beta\varepsilon_{s,cr} \tag{15}$$

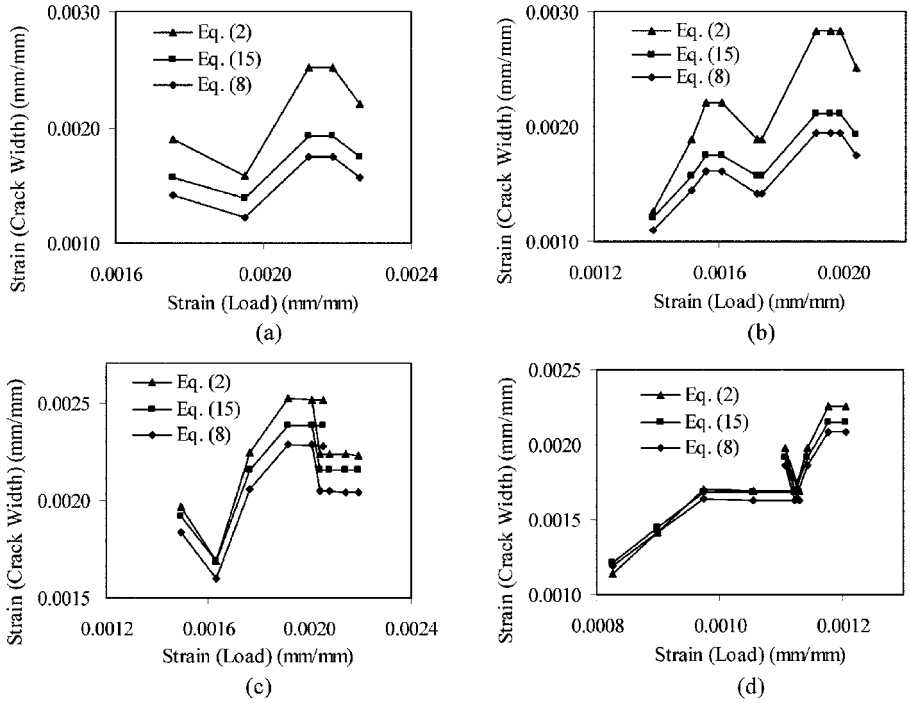

Fig. 3 Strain in reinforcement at a crack calculated using Eq. (2), Eq. (8), and Eq. (15) for (a) Beam 2, Crack 2, (b) Beam 2, Crack 3, (c) Beam 3, Crack 1, and (d) Beam 3, Crack 3

5. Reinforced concrete flexural beams

Four flexural beams were tested under monotonic three-point loading as part of a study to evaluate the crack memory feature of the Teflon sensors (McDaniel 2004). The specimens were 150 mm square and had a span of 910 mm. A Teflon sensor was grouted into a 13 mm square groove on the tension face. Load was applied to the beams in incrementally increasing levels under displacement-control mode. The load, crack width, and reflection coefficient were recorded at each displacement level. The crack width was measured on the side of the beam at the bottom edge using a crack scope. The data from Beam 2 and Beam 3 are included in this paper.

5.1. Model application in flexural beams

Fig. 3 compares ε_{s0} calculated using Eq. (2) (Gergely-Lutz), Eq. (8) (Belarbi-Hsu), and Eq. (15) (CEB-FIP Code) for the flexural beam tests described previously. The ε_{s0} predicted by the three equations are plotted (vertical axes) against the strain calculated from the measured load (horizontal axes) using the procedure described in Section 4. The figure shows that all three equations yield similar results. The sudden jumps in the ordinate values are due to the inherent variability in the crack widths and are exacerbated by being calculated from only one crack measurement taken at each crack during a load increment. Future experimental studies could minimize this problem by averaging multiple crack width measurements along each crack to improve the predicted reinforcement strain.

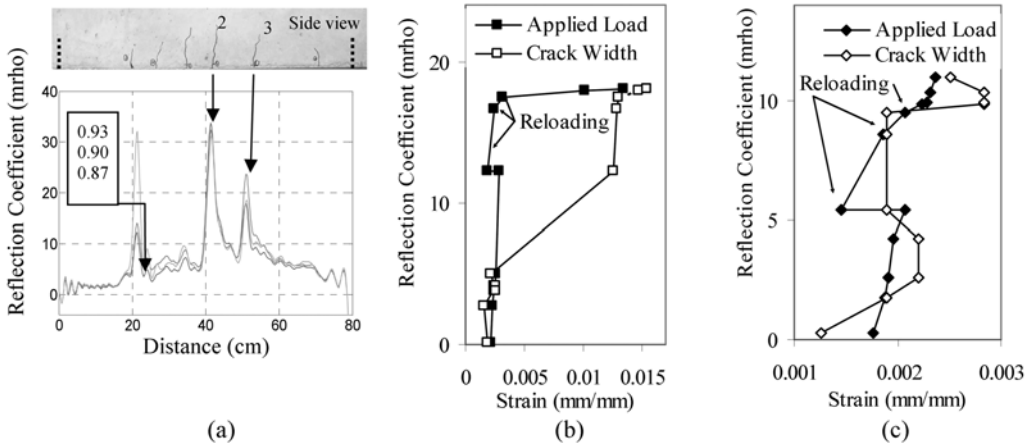

Fig. 4 (a) Beam 2: differenced signals captured at given mid-span deflection (start and end of sensor at dotted lines), (b) sensor response at Crack 2, and (c) sensor response at Crack 3

5.2. Flexural beam sensor response and strain correlation

The process of crack mapping can be improved by using a distributed sensor installed along the entire length of a member. The distributed crack sensors discussed in this paper use the magnitude of the signal's reflection coefficient to monitor crack width and reinforcement strain. The data from the flexural beam tests was used to make a correlation between the sensor response and the reinforcing strain.

Two methods were used to calculate strain in the reinforcing bars at a crack. The first used a measured crack width and the Gergely-Lutz expression given in Eq. (2). For comparison, the reinforcing bars strain at the crack was also calculated using the experimentally measured applied

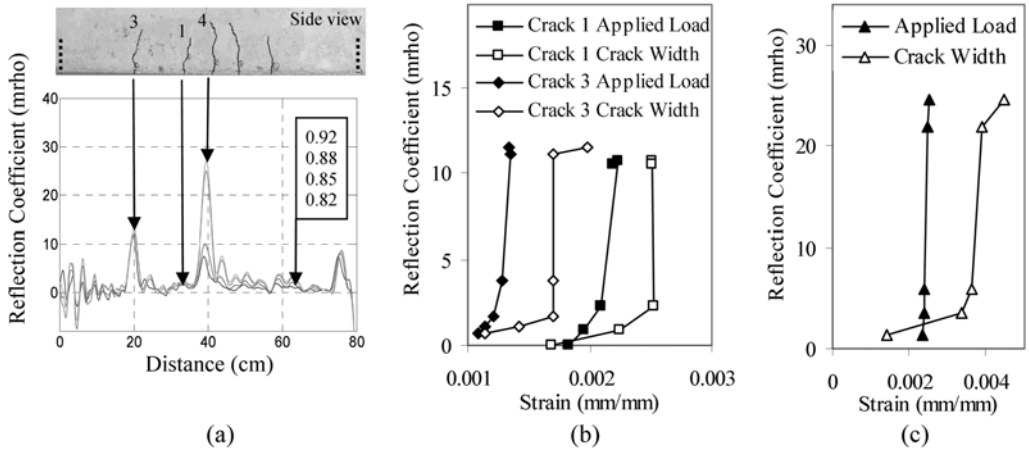

Fig. 5 (a) Beam 3: differenced signals captured at given mid-span deflection (start and end of sensor at dotted lines), (b) sensor response at Cracks 1 & 3, and (c) sensor response at Crack 4

load. First, the average strain in the reinforcing bars was calculated using a stress-block method (Collins and Mitchell 1997). Then, the strain in reinforcing bars at a crack, ε_{s0}, was calculated using Eq. (6).

The reflection coefficients for Beams 2 and 3, calculated from the ETDR differenced signal for given mid-span deflections (in percent of span length), are shown in Figs. 4(a) and 5(a). The reflection coefficients for Cracks 2 and 3 on Beam 2 and Cracks 1, 3, and 4 on Beam 3 are shown versus strain in Figs. 4(b), 4(c), 5(b), and 5(c). The strains calculated from the applied load and calculated from the crack width is shown in these figures.

Beam 2 was partially unloaded immediately before the initiation of yielding of reinforcement. Three data points in Figs. 4(b) and 4(c) are indicated as reloading. Reinforcement yielding in the beam initiated soon after the third reloading point. In Fig. 4(b), a portion of the response which used crack width to calculate the strain is dashed. The beam's load-displacement response indicated that the reinforcement has yielded, and the Gergely-Lutz equation (Eq. 2) does not account for stresses in reinforcing bars beyond yielding. The reinforcing bars were not yielding at Crack 3 of Beam 2 or at Cracks 1, 2, and 3 in Beam 3. The general shape of the sensor response calculated using the applied load is linear for these cracks. Also, Crack 2 of Beam 2 was linear up to yielding. The sensor response calculated using crack width was similar to the applied load response at small strains. At larger strains, the Gergely-Lutz equation overestimated the strain, but this was expected, because the equation was calibrated to give the maximum crack width, and here it is being used to estimate an average crack width. The sensor responses in Figs. 4(b), 2(c), 3(b), and 3(c) show that the reflection coefficients correlate to both the strain in the reinforcing bars and to the crack width.

6. Model for diagonal cracks and orthogonal reinforcement

The previous model considered reinforcement parallel to the direction of the principal tensile strain. In members with an orthogonal grid of reinforcement and inclined cracking, the model described previously requires modification. The panel shown in Fig. 6 is reinforced in the longitudinal and transverse directions indicated by the *L*-*T* axes. Diagonal cracks occur at an angle α to the *L*-axis, at a spacing of *s*, and have a crack width of *w*. These cracks occur normal to the direction of the principal tensile strain, ε_r, and parallel to the principal compressive strain, ε_d. The principal strains are indicated by the *d*-*r* axes in Fig. 6. Using strain transformation, the average strains in the longitudinal and

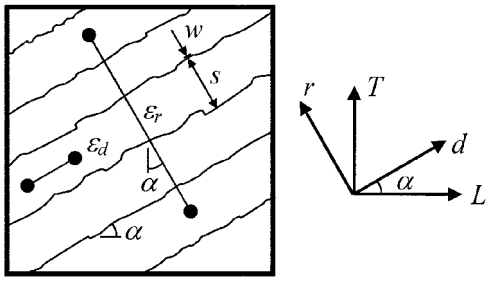

Fig. 6 Panel with diagonal cracking and coordinate system

transverse direction, ε_L and ε_T respectively, can be calculated based on the principal strains and the angle α, ε_d, ε_r, ε_L, and ε_T. The average strains ε_L and ε_T are considered to be the average strains in the longitudinal and transverse reinforcement respectively.

Methods to calculate ε_r using measured crack width were described previously; however calculating ε_d by making measurements on an in-situ structure is not practical. Even in the laboratory, compressive strain calculated from measurements is subject to large scatter (Belarbi and Hsu 1995). Instead, by noticing that ε_d is much less than ε_r for RC members, then ε_d can be neglected. Thus, Eqs. (16) and (17) for the average strain in the reinforcement can be given as

$$\varepsilon_L = \varepsilon_r \sin^2(\alpha) \tag{16}$$

$$\varepsilon_T = \varepsilon_r \cos^2(\alpha) \tag{17}$$

The concept of strain transformation should also be true for the strain in the reinforcement at the crack. As noted previously, $\varepsilon_r = \varepsilon_s$ for the case where the reinforcement is not yielding, so Eqs. (16) and (17) and can be modified to calculate the stress in the reinforcement at a crack. Eqs. (18) and (19) give the reinforcement sttrain at a crack in the longitudinal and transverse directions, ε_{L0} and ε_{T0} respectively.

$$\varepsilon_{L0} = \varepsilon_{s0} \sin^2(\alpha) \tag{18}$$

$$\varepsilon_{T0} = \varepsilon_{s0} \cos^2(\alpha) \tag{19}$$

7. Reinforced concrete girders under combined shear and torsion

In order to interpret the results of this study, understanding the behavior of RC members under loads that induce significant shear stresses is necessary. The shear stress from the applied torsion flows around the box-girder and will combine with the shear flow induced by the applied vertical load. In one vertical face, the two components of shear flow are additive, while their net effect is less in the opposite face. Diagonal cracks occur normal to the direction of the principal tensile stress when the concrete's tensile strength is exceeded, forming concrete compressive struts between the cracks. A component of the shear stress acts in compression through the concrete struts and another component acts in tension through the longitudinal and hoop reinforcing steel. The tensile strains in the longitudinal steel will vary from a maximum at the crack, to a minimum between the cracks where part of the tension force is taken by the concrete. Even after cracking, the concrete between the diagonal cracks continues to provide stiffness to the beam, although to a lesser extent. The phenomena of the concrete adding to the girder's stiffness in the principal tensile direction is known as tension stiffening, and has been investigated by many researchers (Vecchio and Collins 1986, Belarbi and Hsu 1994, and Belarbi and Hsu 1995).

7.1. Reinforced concrete girder test description

This was the second large-scale girder of an ongoing research program to investigate RC girders under cyclic combined shear and torsion (Belarbi and Greene 2004). The cable sensor was a

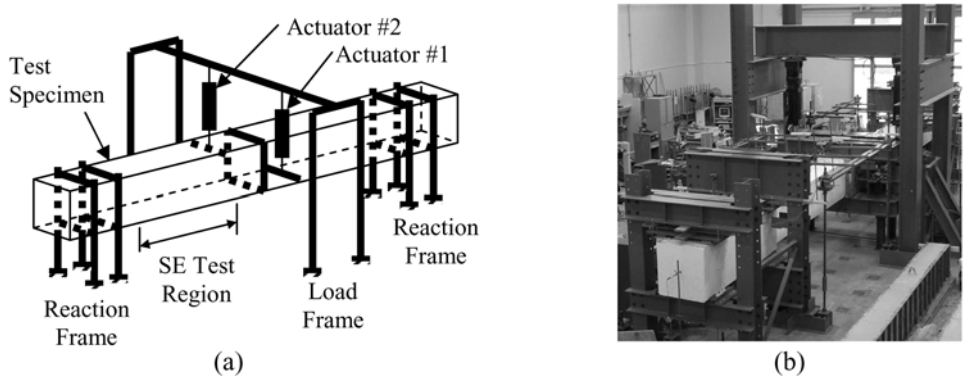

Fig. 7 (a) Schematic test setup for combined torsion-shear-bending loading and (b) test setup photo

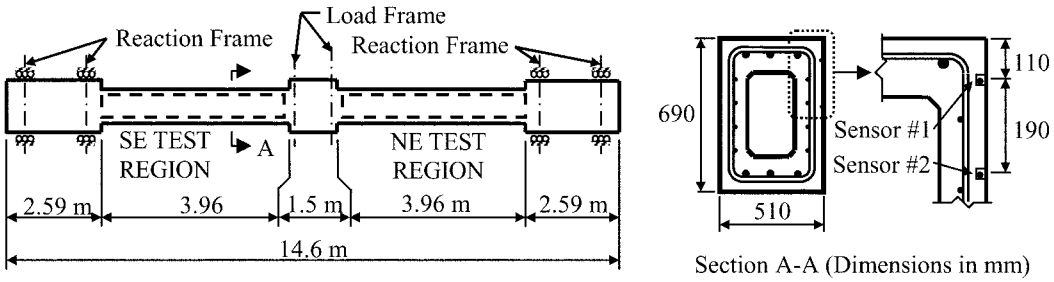

Fig. 8 Test setup – side view, cross section, and sensor locations

natural addition to this study to investigate new technologies for continuous health monitoring. The test setup for this investigation was designed to create constant shear and torsion in the test region. At the same time, the moment was minimized by creating a point of zero moment near the middle of each test region. The shear flow caused by the applied torsion and shear was additive in the southeast (SE) and northeast (NE) test regions. Fig. 7 shows a schematic and photo of the test setup.

The loading was applied to the girder using two servo-controlled hydraulic actuators. Two triangular reaction frames at the middle of the girder prevented the girder from moving either longitudinally or transversely, but permitted vertical and rotational movement. Two additional reaction frames at each end were used for transferring both torsion and vertical loads to the strong-floor, but had rollers to allow the specimen to freely move longitudinally.

The 14.6 m long girder had a 690 mm by 510 mm wide hollow cross-section in the test regions as shown in Fig. 8. The specimen was enlarged at the ends to force failure in the test regions. Longitudinal reinforcement was placed in top and bottom flanges and the two webs and closed stirrups were spaced every 150mm in the test regions. Electronic strain gages were placed throughout the specimen and the gages on longitudinal bars were designated SEL and the gages are on stirrups are SET. Additional instruments were attached to middle of the girder test regions to measure smeared concrete strain in the vertical, horizontal, and diagonal directions. Two 9 m long Teflon sensors were imbedded in the test regions as shown in Fig. 8. The sensors were grouted into 13 mm square grooves that were cast into the girder.

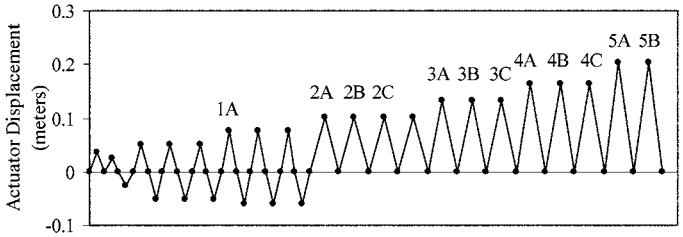

Fig. 9 Applied loading cycles

The girder was subjected to twenty combined shear and torsion cycles, the first seven of which were full reversal cycles. The loading was applied in seven groups. The first group cracked the girder. Group 3 was the last of four load groups after cracking but before the onset of yielding. Yielding initiated during Group 4, and the applied load reached its peak during Group 5. The magnitude of the loading was maintained within the group but was increased at the beginning of a subsequent group. During the first five loading groups the actuators were in force-controlled mode until the peak load for that cycle was reached, at which time the actuators were changed to displacement-controlled mode. In the last two load cycle groups (Groups 4 and 5) the load was applied in displacement control during the entire time to control girder movement after the onset of yielding of reinforcement. Fig. 9 shows the applied load as measured by the displacement of south actuator. This actuator applied a larger force than the north actuator in order to create combined torsion/shear loads in the beam. Loading Groups 1 through 5 are shown and the letters designate the first, second, and third cycle of each group. The ratio of the applied torque to shear loading was maintained near 500mm during all twenty cycles. The peak load was held constant during each cycle to make ETDR measurements, mark cracks, and take photos.

7.2. Reinforced concrete girder behavior

Loading Groups 1, 2, and 3 occurred after cracking but before the onset of yielding. The crack widths, throughout the test region, were relatively uniform through the end of Group 3. The girder reinforcement yielded during Cycle 4A, and small localized areas in the corners of the SE and NE test regions near the middle of the specimen showed signs of spalling. The actuator displacements in Cycle 4B and 4C were set to match those of 4A. During Cycles 4B and 4C, the number and size of the spalled

Fig. 10 SE test region after Load Cycle 4C

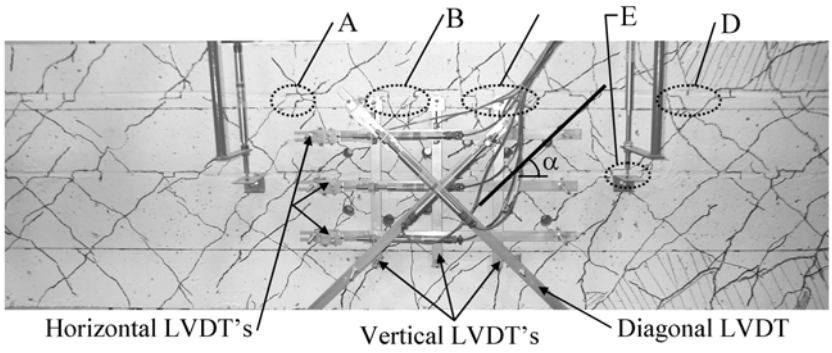

Fig. 11 SE test region – crack group locations and LVDT's for SCSS

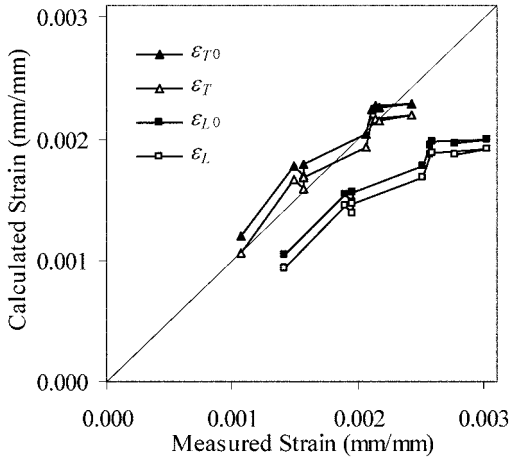

Fig. 12 Calculated versus measured strain for longitudinal and transverse reinforcement

regions grew with each cycle, and the cracks became wider near the middle of the girder, and closed somewhat in the middle of the test regions. The additional cracks and spalling reduced the girder's stiffness and less actuator force was needed in Cycles 4B and 4C to produce the same displacements as in Cycle 4A. The peak applied load occurred during Cycle 5A, and significant portions of the concrete in the top flange and web near the middle of the specimen had spalled. The final cycle, 5B, showed a significant reduction in strength before crushing of concrete occurred in the web of the NE test region.

Fig. 10 shows the SE test region during Cycle 4C at its peak load. Spalled regions were indicated with hatch marks on the specimen. The locations of Sensors #1 and #2 are indicated in this figure and beginning point of the cable is also shown. Fig. 11 shows an enlarge photograph of the SE face during Cycle 4C and gives the location of the five groups of cracks investigated in this paper. Crack Groups A, B, C, and D are along Sensor #1 and Crack E is along Sensor #2.

7.3. Model application in girder

Fig. 12 shows the strain calculated using Eqs. (16-19) plotted versus the strain measured by strain gages. ε_r used in Eqs. (16) and (17) was calculated using the LVDT's in the horizontal, vertical, and

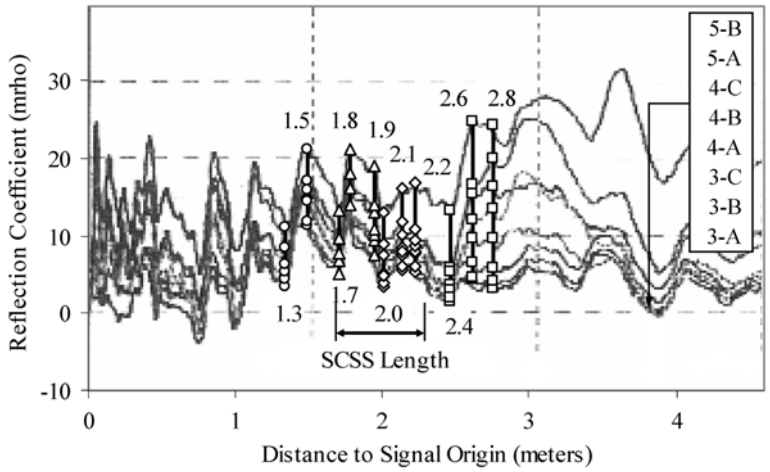

Fig. 13 Differenced signal from Sensor #1 – SE test region

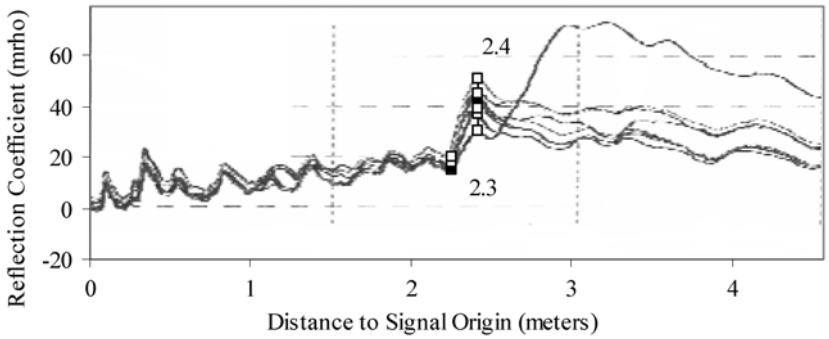

Fig. 14 Differenced signal from Sensor #2 – SE test region

diagonal directions shown in Fig. 11 and by using a measured diagonal crack angle, α, of 43°. The longitudinal strain was measured using one gage, SEL4B, and the transverse strain was measured using the average of four gages, SET1 through SET4. Fig. 12 shows a comparison between the measured and calculated strain in the transverse reinforcement where multiple strain gages were used for the measurement. The figure also shows a comparison of the average reinforcement strains (ε_L and ε_T) and the reinforcement strains at a crack (ε_{L0} and ε_{T0}).

7.4. Reinforced concrete girder sensor response

The strain and reflection coefficient data from the girder test was used to make a correlation between the sensor response and the reinforcement strain for members with diagonal cracking and orthogonal reinforcement. The reflection coefficients calculated from the ETDR differenced signal are shown in Fig. 13 for the data taken during the peak of the last eight cycles from Sensor #1. The ETDR signal originated from the left end of the cable. The peaks indicate crack locations and the magnitude of the reflection coefficient indicates the level of disturbance in the cable. There are multiple sharp peaks near the origin of the signal and less pronounced peaks further from the signal origin due to signal loss

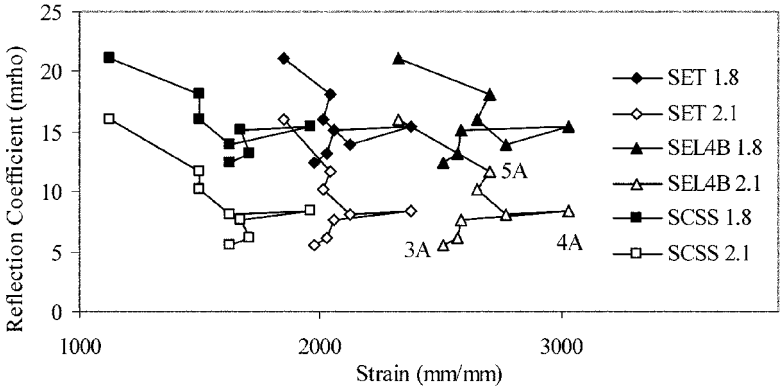

Fig. 15 Strain measurements versus sensor reflection coefficient

(attenuation). Fig. 13 also shows the location of crack Groups A, B, C, and D and their distances from the sensor origin. The position and gage length of the horizontal LVDT's used in the smeared concrete strain sensors (SCSS) are also indicated in the figure.

The reflection coefficient for the first 4.6 m of Sensor #2 is shown in Fig. 14. Along the first 2.3 m of Sensor #2, very few sharp peaks developed in the signal. Examination of the sensor after the completion of the test showed that the grout used to bond the sensor to the specimen was significantly stronger in tension than the grout used for Sensor #1. This result indicated that the grout was too strong to allow the cracks that formed in the specimen to be developed in the grout and then detected by this sensor. The peak that developed at 2.4 m in Sensor #2 was due to the same diagonal crack that caused peak at 2.8 m in Sensor #1 (Crack D).

An electromagnetic wave traveling in a coaxial cable attenuates as it travels along the cable. The loss in signal strength will reduce the spatial resolution and sensitivity of the cable and reduces its effectiveness as a distributed sensor (McDaniel 2004). This effect of attenuation in Sensor #1 can be seen in Fig. 13 as sharp peaks over the first several meters transition to much wider peaks near the middle of the girder. The cable in the NE test region is too far from the signal origin to act as a sensor. The signal from Sensor #2 also shows a slow gradual rise from the signal origin to the crack at 2.4 m due to attenuation.

7.5. Reinforced concrete girder sensor-strain correlation

The strain gage SEL5T is near Crack A; SEL4B, SET and the SCSS are near crack Groups B and C; and SEL3B and SEL3T (SET3) are near Groups D and E. Fig. 15 shows the reflection coefficients from the first crack of Groups B and C plotted versus the strain gages on longitudinal bars, on stirrups, and from the SCSS. Fig. 15 lists the strain measurement designation followed by the crack's distance from the signal origin in meters and also indicates the load group. The general shape of response is the same using all three types of strain measurement, so all further comparisons will be made using strain gages on longitudinal reinforcing bars.

The lowest point in each curve in Fig. 15 is from load Cycle 3A. The Group 3 load was applied in force-controlled mode, therefore the strain increased slightly in Cycles 3B and 3C with a corresponding increase in reflection coefficient and crack width. The magnitude of the applied load was greater in Group 4A than in Group 3, and the responses show an increase in strain and crack width. The increase

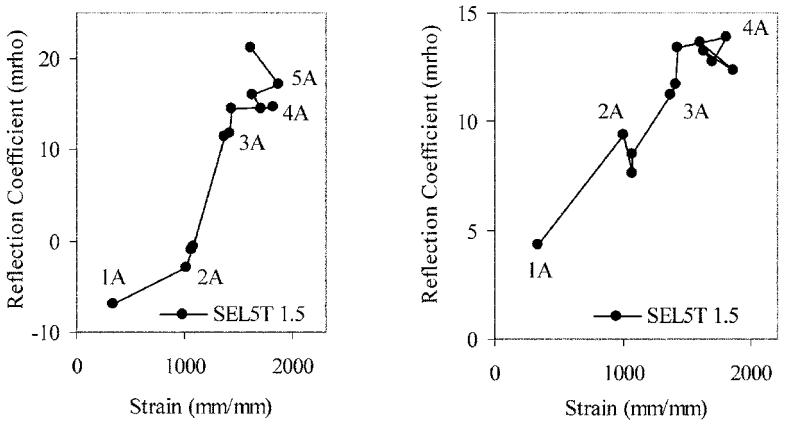

Fig. 16 (a) Crack A total reflection coefficient and (b) Crack A effective reflection coefficient

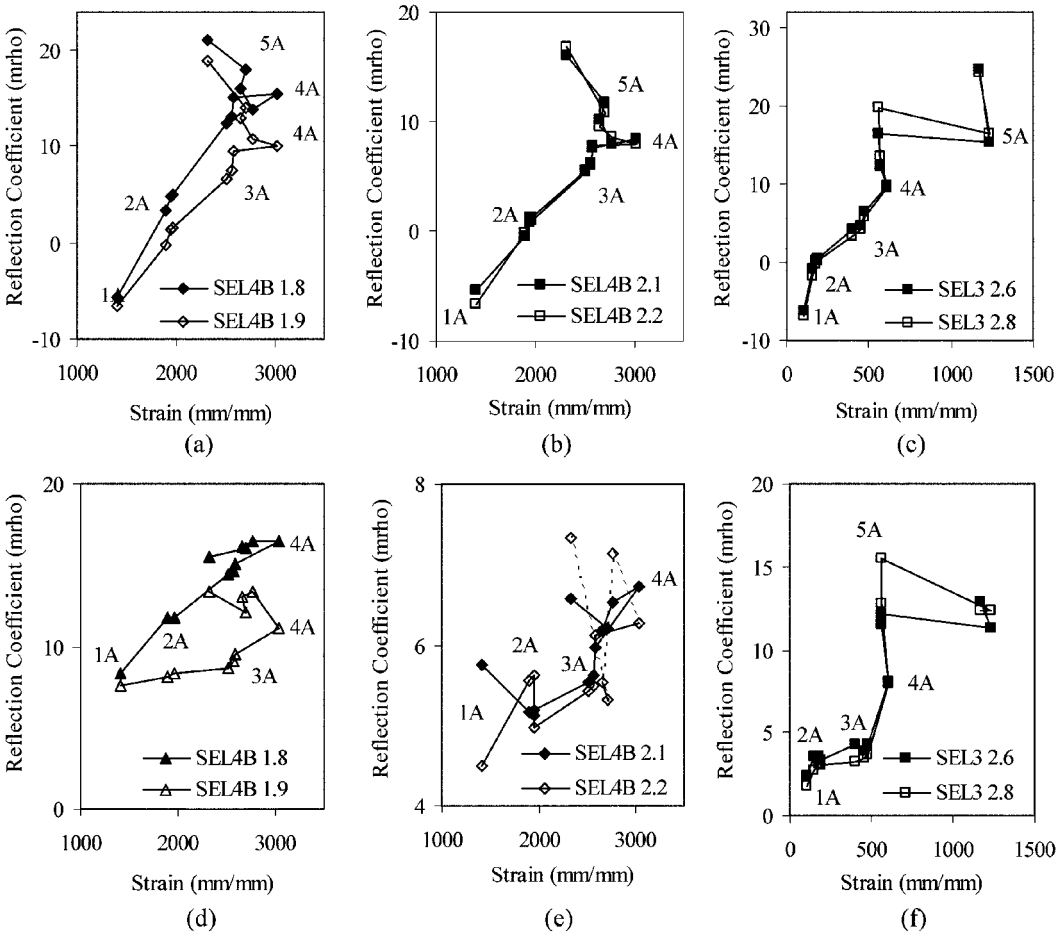

Fig. 17 Total reflection coefficient: (a) Crack Group B, (b) Crack Group C, and (c) Crack Group D; and effective reflection coefficient: (d) Crack Group B, (e) Crack Group C, and (f) Crack Group D

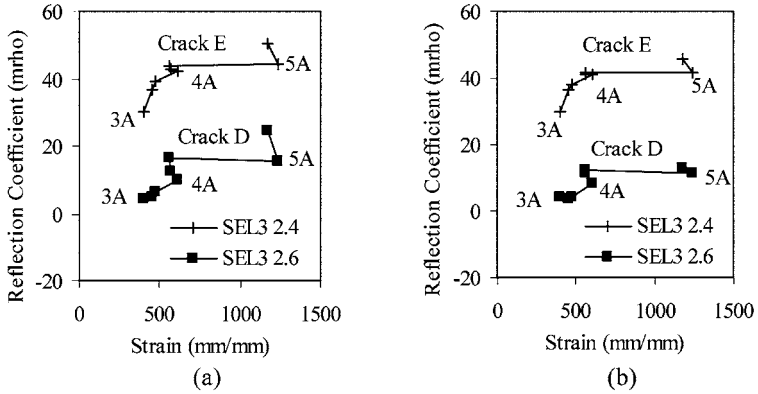

Fig. 18 (a) Total and (b) effective reflection coefficient for Cracks D and E

in crack width and a decrease in strain associated with Cycles 4B and 4C are due to the displacement-controlled loading and girder's reduced stiffness. The repeated cycles caused some additional concrete to spall, and also continued to widen the crack openings, which softened the concrete's compressive strength. Since the girder's reduced stiffness required less force to cause the same rotation and displacement, the stress in the reinforcing bars was also reduced. Cycle 5A was again at a higher load, and so both the strain and reflection coefficient increase together. The spalling that occurred during Cycle 5A weakened the girder considerably and the strain in Cycle 5B is reduced while the reflection coefficient was considerably higher.

Fig. 16(a) shows the response from Crack A plotted against the strain from SEL5T. The response for Crack A was similar to the general response discussed above after Cycle 3. Fig. 16 includes the sensor response from Cycles 1A, 2A, 2B, and 2C. The response is nearly linear before the reinforcement yields during Cycle 4A. The response for crack Groups B, C, and D are shown in Figs. 17(a), 17(b), and 17(d). Crack Groups B, C, and D, each had multiple peaks, with the response from the first crack "spilling over" and affecting the second peak. The reflection coefficients of the two responses in each group were similar for Groups C, and D. The reflection coefficients in the second crack of Group B were all lower than the first crack, but the general shape of the cracks was similar. Until the onset of yielding in Cycle 4A, the response for the first and second crack of Groups B, C, and D were similar and nearly linear.

The response for crack Group D differs from the previous ones. Its response is nearly linear up to 4A, however from 4A to 4C the response remains linear but changes directions and becomes nearly vertical. This change in response is due to the additional bending moment at the location of the crack. Whereas the previous crack groups were in a region of the beam dominated by shear stresses, crack Group D is closer to the middle of the girder where there is a considerable bending moment in addition to shear. The bottom longitudinal bar yielded during the fifth cycle causing the large shift in the strain for the last two points. This crack group does not exhibit the spill-over effect seen in the previous groups. More testing will be required to determine if this is due to crack Group D being in a moment dominated region of the girder. The general shape of the response for Crack E is similar to that of Crack D as shown in Fig. 18(a). This shows that two different sensors respond to a given crack in a similar manner.

By comparing Figs. 17(d), 17(e), and 17(f), it can be seen that the reflection coefficient cannot

be modeled by a unique function of the strain. There are two main reasons for this. First, the width of a particular crack is affected by both the strain and the spacing between cracks as described by Eq. (7). Second, the reflection coefficient in one crack is affected by its proximity to adjacent cracks (spill-over). In future studies, the cracking in simply supported beams will be controlled to study the reflection coefficient-strain response of single and multiple cracks. This will allow a model of the reflection coefficient to be developed which can account for the interaction of multiple cracks.

7.6. Effective reflection coefficient

The reflection coefficient signal does not recover after some peaks and return to the previous baseline. Instead, the shape of reflection coefficient data maintains a similar shape to the data in the previous load cycles, but is offset by a continuous amount.

Because of this, the reflection coefficients at later points along the sensor are a combination of local effects and previous disturbance to the sensor. To account for this, an effective reflection coefficient was calculated by adding the difference between the reflection coefficient of the peak and the previous valley to the lowest value of the previous valley. In Fig. 13 for example, there is a large offset in the sensor data for Cycle 5A right before the crack at 2.6m. Cycle 5A effective reflection coefficient for this crack would be calculated by taking difference between Cycle 5A reflection coefficients from the crack at 2.6 m and the valley at 2.4 m and adding it to the value from the valley of Cycle 3A at 2.4 m.

Fig. 16(b) shows the effective reflection coefficient response for Crack A. The shape of the curve from Cycle 1A until 4A is nearly identical to the response shown in Fig. 16(a) using the total reflection coefficient values. All of the strain and effective coefficients from Cycles 4B to 5B are less than Cycle 4A, giving an indication of the occurrence of unloading. The effective response for crack Group B is shown in Fig. 17(d). The first crack at 1.8m shows a fairly linear response from Cycles 1A to 4A when the applied force increases with each cycle, and shows then a nearly linear unloading response from Cycles 4A to 5B when the force was mainly decreasing with each cycle. Also, the slope from Cycle 4A to 5B is less indicating a decrease in the system's stiffness. The second crack in Group B at 1.9m shows a similar response until Cycle 4A. The response after Cycle 4A is less regular and shows considerable spill-over affect from the first crack. Fig. 17(e) shows the effective responses for the two cracks in Group C. Again, the response for the first crack is nearly linear up to Cycle 4A and shows a reduced slope back to Cycle 5B. The spill-over from the first crack has a strong affect on the second crack after Cycle 4A. The effective response for Group D is shown in Fig. 17(f). The similarity to the total response illustrated in Fig. 17(e) shows that there is minimal spill-over between the two cracks. The total reflection coefficient shown for Cycle 5B is considerably higher than that of Cycle 5A, while the difference between the effective reflection coefficients for the same two cycles is considerably less. This shows that the reflection coefficient data for Cycle 5B had not recovered from disturbances that occurred closer to the signal origin. By using the effective reflection coefficient, the effect of the data offset can be reduced. As shown in Figs. 18(a) and 18(b) the shape and reflection coefficient values for the total and effective response of Crack E are similar. This is expected because the crack at 2.4m along Sensor #2 was the first major peak in the data.

8. Conclusions

A model for predicting the reinforcement strain based on crack mapping was developed. The model could be used to predict the reinforcement strain in a member under direct tension and/or flexural tension up to yielding of reinforcement. The model could also be used to predict the reinforcement strain in the web of a beam under shear stresses where the cracks are inclined angle to the reinforcing bars.

This paper also described the application of distributed coaxial crack sensors for crack mapping and calculating strain in the reinforcement. This was the first step towards relating the reflection coefficient from a distributed coaxial crack sensor to crack width and strains in an RC member. The results discussed in this paper showed that this type of sensor has very promising potential. The following conclusions are made from the sensor results discussed previously:

The cable sensors are capable of capturing crack locations, and changes in the magnitude of the reflection coefficient show increases in crack width due to strain in the member from increases in applied load.

Up to yielding of reinforcement, relationship between reflection coefficient and the strain in the reinforcing bars is nearly linear. After yielding, the relationship is dependent on the way the load is applied, and softening in the beam caused by cracking and spalling.

Multiple cracks distributed along the length of the sensor produce a similar reflection coefficient response. A single crack passing two separate sensors cause a similar response in each sensor.

The effective reflection coefficient discussed herein is capable of identifying crack responses affected by spill-over from previous cracks. It can also remove the signal offset caused by disturbance to the sensor that occurred closer to the signal source.

The crack responses using either the total reflection coefficient or the effective reflection coefficient were significantly different before and after the initiation of yielding. Also, local yielding was distinguishable from global yielding in the girder.

References

Beeby, A. W. (1972), "A study of cracking in reinforced concrete members subjected to pure tension", Technical Report 42.468, Cement and Concrete Association, London.

Belarbi, A. and Greene, G. (2004), "Reinforced concrete box girders under cyclic torsion", *Proceedings 13th World Conference on Earthquake Engineering.*, Vancouver, B.C., Canada, August, Paper No. 998.

Belarbi, A. and Hsu, T. T. C. (1994), "Constitutive laws of concrete in tension and reinforcing bars stiffened by concrete", *ACI Struct. J.*, **91**(4), 465-474.

Belarbi, A. and Hsu, T. T. C. (1995), "Constitutive laws of softened concrete in biaxial tension-compression", *ACI Struct. J.*, **92**(5), 562-573.

CEB-FIP (1993), *Model Code 1990: Design Code*, Comité Euro-International du Béton, London.

Chen, G., Mu, H., Pommerenke, D. and Drewniak, J. L. (2004), "Damage detection of reinforced concrete beams with novel distributed crack/strain sensors", *J. Struct. Health Monitoring*, **3**(3), 2004, 225-243.

Chen, G., Sun, S., Shen, X., Pommerenke, D., Greene, G., Belarbi, A. and Mu, H. (2003), "Crack detection of a 15 meter long reinforced concrete girder with a single distributed cable sensor", *Proceedings of the 1st International Conference on Structural Health Monitoring and Intelligent Infrastructure*, Tokyo, Japan.

Collins, M. P. and Mitchell, D. (1997), *Prestressed Concrete Structures*, Response Publications, Ontario, Canada.

Gergely, P. and Lutz, L. A. (1968), "Maximum crack width in reinforced concrete flexural members", *Causes, Mechanisms, and Control of Cracking in Concrete*, SP-20, ACI, Detroit, 87-117.

Leonhardt, F. (1977), "Crack control in concrete structures", IABSE Surveys, S-4/77, IABE Periodical 3/1977, International Association for Bridge and Structural Engineering, Zurich, Switzerland.

Lin, M.W., Abatan, A.O., and Zhou, Y. (2000), "Transverse shear response monitoring of concrete cylinder using embedded high-sensitivity ETDR sensors", *Smart Structures and Materials 2000: Smart Systems for Bridges, Structures, and Highways; Proceedings of 7th SPIE*, Newport Beach, California.

McDaniel, R. D. (2004), "Characterization and implementation of distributed coaxial cable crack sensors for embedment in reinforced concrete structural members", M.S. Thesis, UMR, Rolla, Missouri.

Rizkalla, S. H., Hwang, L. S. and El Shahawi, M. (1983), "Transverse reinforcement effect on cracking behavior of RC members", *Canadian J. Civ. Eng.*, **10**(4), 566-581.

Vecchio, F. J. and Collins, M. P. (1986), "The modified compression field theory for reinforced concrete elements subject to shear", *ACI J.*, **83**(2), 219-231.

CC